

Photovoltaic properties of $ABSe_3$ chalcogenide perovskites ($A = Ca, Sr, Ba$; $B = Zr, Hf$)Surajit Adhikari^{✉*} and Priya Johari^{✉†}*Department of Physics, School of Natural Sciences,**Shiv Nadar Institution of Eminence, Greater Noida, Gautam Buddha Nagar, Uttar Pradesh 201314, India*

(Received 24 January 2024; revised 4 April 2024; accepted 2 May 2024; published 20 May 2024)

Lead-free, stable photovoltaic materials with promising optoelectronic features have recently been discovered in chalcogenide perovskites. However, a thorough theoretical analysis of excitonic and polaronic properties has never been done because it would require enormous computing. Here, we elucidate the role of excitonic and polaronic effects in a sequence of chalcogenide perovskites $ABSe_3$ ($A = Ca, Sr, Ba$; $B = Zr, Hf$), including their needlelike (α -phase) and distorted (β -phase) structures, along with their relative stability and optoelectronic properties by employing state-of-the-art density functional theory, density functional perturbation theory (DFPT), and many-body perturbation theory [GW and Bethe-Salpeter equation (BSE)]. We find all the investigated perovskites to be dynamically as well as mechanically stable and possess direct electronic (G_0W_0) band gap in the range of 1.02–1.97 eV. We investigate the interplay of the ionic and electronic components of the dielectric screening through the DFPT and BSE methods and find that the electronic component predominates. Interestingly, they exhibit smaller exciton binding energy (0.02–0.10 eV) than conventional halide and sulfur-based chalcogenide perovskites. The polaronic mobility for electrons (holes) is in the range of 8.26–77.59 $\text{cm}^2\text{V}^{-1}\text{s}^{-1}$ (19.05–100.49 $\text{cm}^2\text{V}^{-1}\text{s}^{-1}$), which also found to be much higher than that of sulfur-based chalcogenide perovskites, owing to less carrier-phonon interactions in the former. All the examined properties suggest β - $ABSe_3$ to be promising environmentally friendly stable materials for photovoltaic applications. This has been further confirmed by estimating spectroscopic limited maximum efficiency, which is calculated as $\sim 17.5\%$ – 23% for these materials.

DOI: [10.1103/PhysRevB.109.174114](https://doi.org/10.1103/PhysRevB.109.174114)**I. INTRODUCTION**

The popularity of inorganic-organic halide perovskites (IOHPs) in the area of solar cells has surged over the past few years due to their record power conversion efficiencies (from 3.8% to 25.5%), coupled with cost-effective fabrication techniques [1–4]. However, a significant drawback lies in the majority of these IOHPs being lead (Pb) based, leading to concerns about toxicity, and degradability, thermal as well as chemical instability stemming from the organic component. These factors have become substantial barriers to their effective large-scale industrial applications [5,6].

In response to these challenges, there has been a growing impetus among researchers to redirect their focus toward a distinctive class of perovskites, namely, chalcogenide perovskites (CPs) [7–10], which are Pb free, plentiful on Earth, and extremely stable in the ambient environment compared to their halide counterparts. Other than these, CPs have demonstrated favorable properties such as high absorption coefficients, adequate defect tolerance, promising electronic characteristics, and desirable charge carrier mobility [11–14]. Notably, CPs predominantly consist of ecologically benign Group-IIA (Ca, Sr, and Ba) and Group-IVB (Ti, Zr, and Hf) elements, further enhancing their suitability for large-scale industrial production of efficient solar cells.

The chemical composition of CPs, resembling typical three-dimensional halide perovskites (HPs), is denoted as ABX_3 [13,15], where A and B represent divalent alkali-earth metal cation (Ca^{2+} , Sr^{2+} , and Ba^{2+}) and tetravalent transition metal cation (Ti^{4+} , Zr^{4+} , Sn^{4+} , and Hf^{4+}), respectively, and X generally refers to a chalcogen anion either S^{2-} or Se^{2-} . Two distinct phases of chalcogenide perovskites have been identified at ambient temperature: one is the needlelike orthorhombic phase (NH_4CdCl_3 -type) and another is the distorted orthorhombic structure (GdFeO_3 -type), both sharing the same space group $Pnma$ (No. 62) [13,15].

To the best of our knowledge, to date a few sulfide-based CPs have already been experimentally synthesized, for example, the distorted phase [16] of CaZrS_3 , SrZrS_3 , BaZrS_3 , CaHfS_3 , SrHfS_3 , and BaHfS_3 , and the needlelike phase [17] of SrZrS_3 , while, in addition, several first-principles based studies have been conducted that predict CPs to exhibit promising electronic and optical properties for photovoltaic applications [14,18]. But, on the other hand, higher exciton binding energy (0.19–0.54 eV) and lower charge carrier mobility (6.84–18.77 $\text{cm}^2\text{V}^{-1}\text{s}^{-1}$) than the conventional HPs due to the presence of prominent polaronic effects [14,18], pose a major challenge before relative effectiveness of CPs in solar cells as both of these factors strongly affect the performance of a solar cell. Thus CPs with low exciton binding energy and high polaronic charge carrier mobility need to be explored to address these issues.

In that effort, Sun *et al.* theoretically studied crystal structure and band structure of the needlelike and distorted phases

*sa731@snu.edu.in

†priya.johari@snu.edu.in

of sulfide as well as selenide-based ABX_3 ($A = \text{Ca, Sr, Ba}$; $B = \text{Zr, Hf}$; $X = \text{S, Se}$) CPs [13] and, on the basis of band gap, they predicted selenide-based CPs to be potential substitutes for sulfide-based CPs for the application in solar cells. To date, only needlelike orthorhombic structure of $\text{Sr}(\text{Zr, Hf})\text{Se}_3$ has been successfully synthesized [19,20], while Zr-based CPs have received a selective theoretical attention, mainly restricted to the study of electronic structure properties [15,21,22]. This calls for a thorough understanding of both Zr- and Hf-based $AB\text{Se}_3$ CPs, which has not been achieved yet and is offered here.

In this paper, we have therefore performed a systematic and comprehensive study of electronic, optical, transport, excitonic, and polaronic properties of chalcogenide perovskites $AB\text{Se}_3$ ($A = \text{Ca, Sr, Ba}$; $B = \text{Zr, Hf}$), including their needlelike (α phase) and distorted (β phase) phases within the framework of density functional theory (DFT) [23,24], density functional perturbation theory (DFPT) [25], and many-body perturbation theory (MBPT) [26,27] based GW and BSE. Our results reveal that all investigated CPs have direct band gaps and β phases have band gaps in the visible range (1.69–1.97 eV) compared to the α phases. These materials possess small exciton binding energy (0.02–0.10 eV) compared to conventional HPs and sulfur (S)-based CPs [14,18] and β phases have a longer exciton lifetime than the α phases. The impact of electron-phonon interaction on the charge carrier mobility has also been examined and the polaron mobility is calculated using the Fröhlich model. Finally, the quasiparticle (QP) band gap and absorption coefficient are used to calculate the spectroscopic limited maximum efficiency (SLME) [28], which indicates that β - $AB\text{Se}_3$ are promising materials for photovoltaic applications.

II. COMPUTATIONAL DETAILS

In this paper, the state-of-the-art first-principles density functional theory (DFT) [23,24], density functional perturbation theory (DFPT) [25], and many-body perturbation theory (MBPT) [26,27] based calculations were performed using the Vienna *ab initio* simulation package (VASP) [29,30]. Projector-augmented wave (PAW) [31] pseudopotentials were used to describe the valence electrons and atomic core interactions in all constituent elements. The PAW pseudopotentials with valence state electrons considered for Ca, Sr, Ba, Zr, Hf, and Se were $3s^23p^64s^2$, $4s^24p^65s^2$, $5s^25p^66s^2$, $4s^24p^65s^24d^2$, $5p^66s^25d^2$, and $4s^24p^4$, respectively. The exchange-correlation (xc) functional of Perdew, Burke, and Ernzerhof (PBE), based on the generalized gradient approximation (GGA) [32], was employed for the structural optimization, which takes into account the electron-electron interactions. The kinetic energy cutoff was set at 400 eV for plane-wave basis set expansion to describe the valence electrons. The convergence threshold for the electronic self-consistent-field iteration energy was chosen at 10^{-6} eV. All structures were fully optimized using the PBE functional until the Hellmann-Feynman forces on each atom were less than 0.01 eV/Å. The Γ -centered $13 \times 5 \times 3$ and $7 \times 7 \times 5$ \mathbf{k} -point sampling were applied for Brillouin zone integration in order to determine the optimized needlelike (α -phase) and distorted (β -phase) structures, respectively. The optimized

crystal structures were visualized by electronic and structural analysis (VESTA) [33]. The phonon dispersion curves were calculated based on the density functional perturbation theory (DFPT) [25] with $2 \times 2 \times 2$ supercells, using the PHONOPY [34] package. The band structures were calculated using the PBE xc functional and the spin-orbit coupling (SOC) effect was taken into consideration, though it has no bearing on the trend. The electronic band gaps were also computed simultaneously using the hybrid HSE06 [35] xc functional and many-body perturbation theory (MBPT) based GW [36,37] (G_0W_0 @PBE) method for more accurate estimation. The effective mass was calculated by SUMO [38] using a parabolic fitting of the band edges. We went beyond the HSE06 in order to more precisely determine the optical properties and conducted Bethe-Salpeter equation (BSE) [39,40] calculations on top of the single-shot $GW(G_0W_0)$ @PBE, which specifically takes into account the electron-hole interaction. It should be noted that the GW -BSE calculations were performed using a Γ -centered $3 \times 3 \times 2$ \mathbf{k} grid and a converged NBANDS 640. For the BSE calculations, 24 occupied and 24 unoccupied bands were used to generate the electron-hole kernel. The ionic contribution to the dielectric constant was calculated using density functional perturbation theory (DFPT) [25]. The elastic, electronic, and optical properties underwent post-processing using the VASPKIT [41] package.

The exciton binding energy (E_B) for a screened Coulomb interacting e - h pair is computed by employing the hydrogenic Wannier-Mott (WM) [18,42] model,

$$E_B = \left(\frac{\mu^*}{m_0 \epsilon_{\text{eff}}^2} \right) R_\infty, \quad (1)$$

where μ^* is the reduced mass of the charge carriers, m_0 is the rest mass of the electron, ϵ_{eff} is the effective dielectric constant, and R_∞ is the Rydberg constant. The effective mass has been calculated using the following Eq. [43]:

$$m^* = 3 \left[\frac{1}{m_{xx}^*} + \frac{1}{m_{yy}^*} + \frac{1}{m_{zz}^*} \right]^{-1}, \quad (2)$$

where m_{ii}^* is the effective mass in the i th direction ($i = x, y, z$). The carrier's reduced mass μ^* is provided by

$$\frac{1}{\mu^*} = \frac{1}{m_e^*} + \frac{1}{m_h^*}. \quad (3)$$

The exciton radius (r_{exc}) is calculated as follows [18]:

$$r_{\text{exc}} = \frac{m_0}{\mu^*} \epsilon_{\text{eff}} n^2 r_{\text{Ry}}, \quad (4)$$

where n is the exciton energy level and $r_{\text{Ry}} = 0.0529$ nm is the Bohr radius. In our study, the electronic contribution to the dielectric function (ϵ_∞) is considered as the effective value and $n = 1$, which provides the smallest exciton radius. Using the exciton radius, the probability of a wave function at zero charge separation [$|\phi_n(0)|^2$] is calculated as follows [18]:

$$|\phi_n(0)|^2 = \frac{1}{\pi (r_{\text{exc}})^3 n^3}, \quad (5)$$

In our study, the static dielectric constant (ϵ_s) of these CPs is estimated via

$$\epsilon_s = \epsilon_{\text{elec}}^{\alpha\beta}(\infty) + \epsilon_{\text{ion}}^{\alpha\beta}(\omega), \quad (6)$$

where $\varepsilon_{\text{elec}}^{\alpha\beta}(\infty)$ or ε_{∞} is the electronic component and $\varepsilon_{\text{ion}}^{\alpha\beta}(\omega)$ is the ionic component of the dielectric constant obtained using BSE and DFPT, respectively. The ionic part of the dielectric constant can be derived by the following equation [44]:

$$\varepsilon_{\text{ion}}^{\alpha\beta}(\omega) = \frac{4\pi}{\Omega} \sum_m \frac{S_m^{\alpha\beta}}{\omega_m^2 - \omega^2}, \quad (7)$$

where Ω is the volume of the primitive cell, $S_m^{\alpha\beta}$ is the mode-dependent oscillator strength, ω is the angular frequency, and m represents the phonon normal modes.

The phonon screening correction to the exciton binding energy (E_B) is given by [45]

$$\Delta E_B^{\text{ph}} = -2\omega_{\text{LO}} \left(1 - \frac{\varepsilon_{\infty}}{\varepsilon_s} \right) \frac{\sqrt{1 + \omega_{\text{LO}}/E_B} + 3}{(1 + \sqrt{1 + \omega_{\text{LO}}/E_B})^3}, \quad (8)$$

where ω_{LO} is the characteristic phonon angular frequency and it is evaluated by taking the spectral average of the multiple phonon branches using a thermal “ B ” scheme of Hellwarth *et al.* [46] (for further details, see the Supplemental Material [47]).

In Fröhlich’s polaron model, the longitudinal optical phonons and the electron traveling through the lattice interact via the dimensionless Fröhlich parameter α , which is given as [48]

$$\alpha = \frac{1}{4\pi\varepsilon_0} \frac{1}{2} \left(\frac{1}{\varepsilon_{\infty}} - \frac{1}{\varepsilon_s} \right) \frac{e^2}{\hbar\omega_{\text{LO}}} \left(\frac{2m^*\omega_{\text{LO}}}{\hbar} \right)^{1/2}, \quad (9)$$

where ε_0 is the permittivity of free space and m^* is the carrier effective mass. By knowing α , one can also compute the polaron energy (E_p) by using the expression [14,18]

$$E_p = (-\alpha - 0.0123\alpha^2)\hbar\omega_{\text{LO}}. \quad (10)$$

The effective mass of the polaron (m_p) is also defined using Feynman’s extended version of Fröhlich’s polaron theory (for a small α) as follows [49]:

$$m_p = m^* \left(1 + \frac{\alpha}{6} + \frac{\alpha^2}{40} + \dots \right). \quad (11)$$

Using the Hellwarth polaron model [46], the polaron mobility is defined as follows:

$$\mu_p = \frac{(3\sqrt{\pi}e)}{2\pi c\omega_{\text{LO}}m^*\alpha} \frac{\sinh(\beta/2)}{\beta^{5/2}} \frac{w^3}{v^3} \frac{1}{K(a,b)}, \quad (12)$$

where e is the charge of electron, $\beta = hc\omega_{\text{LO}}/k_B T$, w and v are the temperature-dependent variational parameters, and $K(a,b)$ is a function of β , w , and v (for details, see the Supplemental Material [47]).

III. RESULTS AND DISCUSSIONS

In the present study, we have conducted a systematic and comprehensive investigation of the needlelike (α phase) and distorted (β phase) phases of the chalcogenide perovskites $ABSe_3$ ($A = \text{Ca, Sr, Ba}$; $B = \text{Zr, Hf}$) in order to examine the potential optoelectronic features of these materials. In the following subsections, the stability as well as the structural, electronic, transport, optical, excitonic, polaronic properties, and spectroscopic limited maximum efficiency (SLME) of

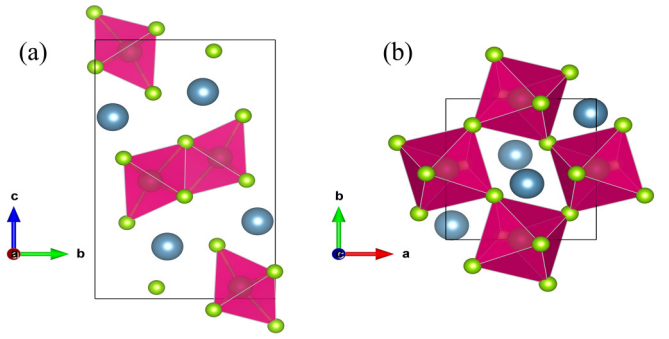


FIG. 1. Crystal structure of the orthorhombic (a) needlelike phase (α phase) and (b) distorted phase (β phase) for CaZrSe_3 chalcogenide perovskite. Cyan, black, and green represent Ca, Zr, and Se atoms, respectively.

$ABSe_3$ CPs are examined and discussed in detail to gain fundamental understanding and to direct future experimental studies.

A. Structural properties

1. Crystal structure

The orthorhombic structures of chalcogenide perovskites $ABSe_3$ ($A = \text{Ca, Sr, Ba}$; $B = \text{Zr, Hf}$) with the space group $Pnma$ (No. 62) are examined in both the needlelike phase (α phase) and the distorted phase (β phase) [14,16–18]. The crystal structures of both the phases are displayed in Fig. 1 and Fig. S1. The crystal structures of these compounds are typically made up of four unit cells having 20 atoms, that include 4 Ca/Sr/Ba, 4 Zr/Hf, and 12 Se atoms. The calculated bond lengths of $ABSe_3$ CPs are given in Table S1. It is observed that the structure of α and β phases are significantly different from each other, despite having the same symmetry. In the β phases, the B -site cations are sixfold coordinated to the Se atoms in a distorted and tilted way, producing corner-sharing distorted octahedrons $[BSe_6]^{8-}$, and cuboctahedrons are formed due to 12-fold coordination of the alkaline earth elements (A -site cations) with the Se atoms (Fig. 1). On the other hand, the coordination number of A -site cations drops from 12 to 9 and the coordination number of B -site cations remains the same (i.e., 6) in the α phase, indicating loss of a few key characteristics of the perovskite structure in the latter [13]. The lattice parameters of the optimized structures are estimated using the PBE xc functional and are listed in Table I. They are found to be in excellent agreement with earlier theoretical and available experimental findings [19–22].

Since the structural stability of perovskites is one of the crucial factors in deciding their high-performance device applications, the crystallographic stability of α and β phases of $ABSe_3$ ($A = \text{Ca, Sr, Ba}$; $B = \text{Zr, Hf}$) CPs is calculated by determining Goldschmidt’s tolerance factor [50,51] (t) and the octahedral factor [51,52] (μ) using the following expressions (for details, see the Supplemental Material [47]):

$$t = \frac{r_A + r_X}{\sqrt{2}(r_B + r_X)}, \quad \mu = \frac{r_B}{r_X}, \quad (13)$$

TABLE I. Calculated lattice parameters of $ABSe_3$ ($A = \text{Ca, Sr, Ba}$; $B = \text{Zr, Hf}$) chalcogenide perovskites.

Configurations	Our study			Previous work			Reference	
	a (Å)	b (Å)	c (Å)	a (Å)	b (Å)	c (Å)		
CaZrSe ₃	α phase	3.88	8.86	14.68				
	β phase	6.85	7.40	10.08	6.85	7.40	10.09	Ref. [22] (Theor.)
SrZrSe ₃	α phase	3.99	9.06	14.63	3.97	8.92	14.51	Ref. [20] (Expt.)
	β phase	7.05	7.51	10.26	7.04	7.52	10.27	Ref. [22] (Theor.)
BaZrSe ₃	α phase	4.06	9.18	15.14	4.08	9.15	15.15	Ref. [21] (Theor.)
	β phase	7.30	7.54	10.49	7.29	7.55	10.50	Ref. [22] (Theor.)
CaHfSe ₃	α phase	3.86	8.87	14.60				
	β phase	6.84	7.34	10.03				
SrHfSe ₃	α phase	3.97	9.04	14.60	3.94	8.90	14.48	Ref. [19] (Expt.)
	β phase	7.04	7.45	10.22				
BaHfSe ₃	α phase	4.04	9.16	15.13				
	β phase	7.28	7.48	10.43				

where r_A , r_B , and r_X are the Shannon ionic radii for A^{2+} , B^{4+} , and X^{2-} ions, respectively. On analyzing the data presented in Table S1, it can be noticed that the t and μ values for all the compounds lie in between 0.828–0.944 and 0.359–0.364, respectively, confirming the stability of needlelike (α -phase) or the distorted (β -phase) perovskite structure for the investigated CPs [15,51,53,54]. A modified tolerance factor has recently been reported by Alexander *et al.* [55] to analyze the phase stability of CPs and further investigate prospective optoelectronic materials. In addition, to determine the thermodynamic stability, the decomposition energy is also computed using the PBE xc functional for these materials (for details, see the Supplemental Material [47]). Nevertheless, these crystallographic and thermodynamic stability are not enough to support their stability; we also assess the dynamical and mechanical stability of these materials.

2. Dynamical stability

To assess the dynamical stability of $ABSe_3$ ($A = \text{Ca, Sr, Ba}$; $B = \text{Zr, Hf}$) CPs, self-consistent phonon calculations are performed using DFPT [25]. Dynamical stability is one of the most crucial indicators of a material's stability since it is connected with the phonon modes. The phonon dispersion curves of α and β phases at $T = 0$ K are shown in Fig. 2 and Fig. S2 (see the Supplemental Material [47]), respectively. For $ABSe_3$ perovskites, the structural symmetry confirms 60 phonon modes corresponding to 20 atoms. Out of these 60 phonon modes, only 3 are acoustic while the rest are optical, and are denoted by low- and high-frequency phonons, respectively. The absence of imaginary frequencies suggests that these perovskites are dynamically stable at $T = 0$ K, in agreement with the prior theoretical work on the α phase of BaZrSe₃ [21] and the β phase of AZrSe₃ ($A = \text{Ca, Sr, Ba}$) [15,56]. The highest optical frequency is found to drop significantly from AZrSe₃ to AHfSe₃.

3. Mechanical stability and elastic properties

In addition to the aforementioned crystallographic and dynamical stability, the mechanical stability and associated elastic properties of $ABSe_3$ ($A = \text{Ca, Sr, Ba}$; $B = \text{Zr, Hf}$) CPs

are also explored. It is well known that the use of a material in practical devices is heavily influenced by its elastic behavior. The energy-strain method [57] is used to calculate the second-order elastic constants (C_{ij}), which finally estimate the elastic properties (for details, see the Supplemental Material [47]). Since all considered CPs have the same orthorhombic symmetry, nine independent elastic coefficients, such as C_{11} , C_{22} , C_{33} , C_{44} , C_{55} , C_{66} , C_{12} , C_{13} , and C_{23} , are sufficient to explain the mechanical stability and corresponding elastic properties of these systems [57,58]. The computed C_{ij} values for each CP are presented in Table S4 and they all satisfy the Born stability criteria [57] (for details, see the Supplemental Material [47]), indicating excellent mechanical stability for these orthorhombic phases of CPs.

Further, the corresponding bulk modulus (B), shear modulus (G), Young's modulus (Y), and Poisson's ratio (ν) are determined according to Voigt-Reuss-Hill approaches [59,60] and are tabulated in Table S4 (for details, see the Supplemental Material [47]). The high values of B relative to G in our study suggest the higher resistance of investigated CPs to volumetric deformation than shape deformation. However, lower values of G and Y indicate that these materials are flexible in nature. It is discovered that the α phase of $ABSe_3$ is a less stiff material than its β phase, except BaHfSe₃. Additionally, Pugh's suggested B/G ratio [61] and Poisson's ratio (ν) are employed to assess the fragility of these materials. The calculated values of B/G (>1.75) and ν (>0.26) imply that all of the considered CPs are ductile materials.

The longitudinal (v_l), transverse (v_t), and average (v_m) elastic wave velocities and the Debye temperature (Θ_D) are also calculated [62] and presented in Table S4 (for details, see the Supplemental Material [47]). Debye temperature (Θ_D) is one of the key factors in determining the thermal characteristics of materials and is strongly related to numerous physical properties, including melting temperature, bond nature, specific heat, and thermal expansion [62,63]. Our investigations reveal that the considered CPs have a relatively low Θ_D value (~ 166 – 262 K), suggesting they are a flexible lattice with low lattice thermal conductivity, which contributes to the high thermoelectric figure of merit [56,62]. The overall mechanical

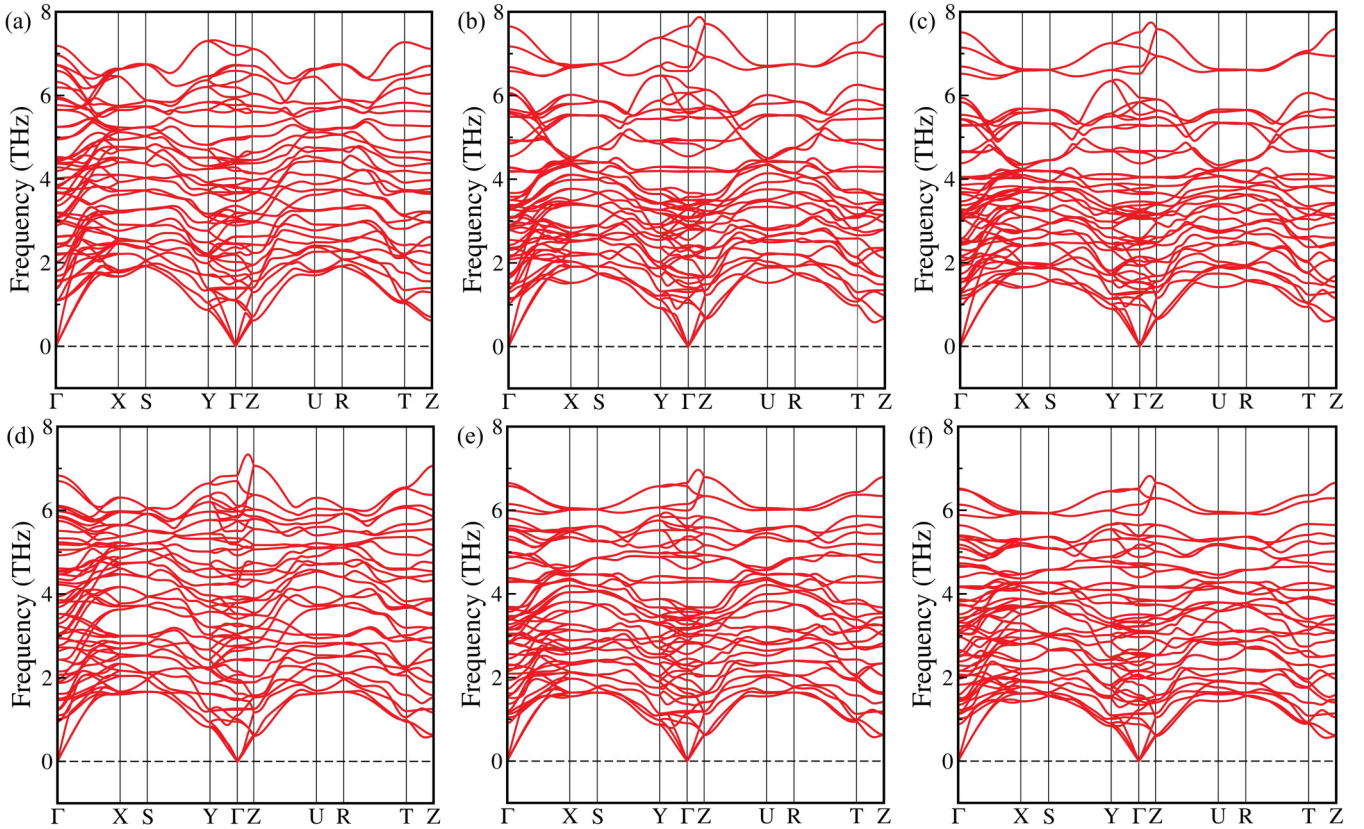


FIG. 2. Phonon dispersion curves of (a) CaZrSe_3 , (b) SrZrSe_3 , (c) BaZrSe_3 , (d) CaHfSe_3 , (e) SrHfSe_3 , and (f) BaHfSe_3 in orthorhombic needlelike (α) phase, calculated with the DFPT method.

studies of these CPs indicate that these materials are promising for flexible optoelectronic and photovoltaic systems.

B. Electronic properties

After ensuring the stability, electronic structure calculations for $ABSe_3$ CPs are carried out since this plays a vital role in designing the photoelectric devices. Here, the partial density of states (PDOS), the total density of states (TDOS), the positions of the band edges, i.e., the conduction band minima (CBM) and the valence band maxima (VBM), as well as the nature of the band gap are estimated to gain deep insights into the electronic structure.

At first, electronic structure calculations for $ABSe_3$ CPs are performed using the most popular semilocal PBE xc functional. However, as it is known that the band gap of chalcogenide perovskites is underestimated by PBE due to the self-interaction error [14,18], a more precise estimation is also made using the hybrid HSE06 [35] xc functional and many-body perturbation theory (MBPT) based GW [36,37] ($G_0W_0@PBE$) method. The band structure computed using the HSE06 xc functional is depicted in Fig. S5 and Fig. 3 for α and β phases, respectively, and it is found that the CBM and VBM for every compound are located at the same \mathbf{k} point (namely Γ point) of the Brillouin zone, which makes them direct band gap materials. Notably, the band structures of $ABSe_3$ CPs obtained using the $G_0W_0@PBE$ method are also given in Fig. S6. The estimated band gap of α and β phases for $ABSe_3$ CPs calculated using the PBE, HSE06 xc functionals,

and $G_0W_0@PBE$ method are tabulated in Table II. It should be noted that spin-orbit coupling (SOC) has not been taken into account as it barely influences the electronic structure of the chalcogenide perovskites [14,18] (for details, see the Supplemental Material [47]). It can be noticed from Table II that the band gap of the β phase is consistently greater than the respective α phase, similar to the previous literature reports [15,18]. The HSE06 ($G_0W_0@PBE$) computed band gap of α and β phases lie in the ranges of 0.86–1.15 eV (1.02–1.26 eV) and 1.42–1.79 eV (1.69–1.97 eV), respectively, optimal for semiconducting applications. These calculated values of the band gap are much lower than their oxide counterpart; for example, the experimental band gaps of CaZrO_3 and SrZrO_3 are 5.7 eV [64] and 5.6 eV [65], respectively. Further, the predicted band gaps of α - BaZrSe_3 and β - AZrSe_3 ($A = \text{Ca, Sr, Ba}$) are well consistent with the previous theoretical results [15,21,22]. Also, the experimental band gap of α - SrHfSe_3 is calculated to be about 1.02 eV [19], which is in good agreement with our HSE06 ($G_0W_0@PBE$) predicted value of 0.99 eV (1.09 eV). The band gaps of β - $ABSe_3$ are also found to be lower than their sulfide counterparts (2.10–2.59 eV) [14,18].

To get profound insights into the electronic structure, the density of states (DOS) calculations using the HSE06 xc functional are also performed and shown in Fig. S3 and Fig. S4. For the α and/or β phase of $AZrSe_3$ ($A = \text{Ca, Sr, Ba}$) perovskites, the VBM is primarily contributed by the $\text{Se-}4p$ orbital, while the CBM is mainly from the $\text{Zr-}4d$ orbital, along with minor contributions from the remaining orbitals made at

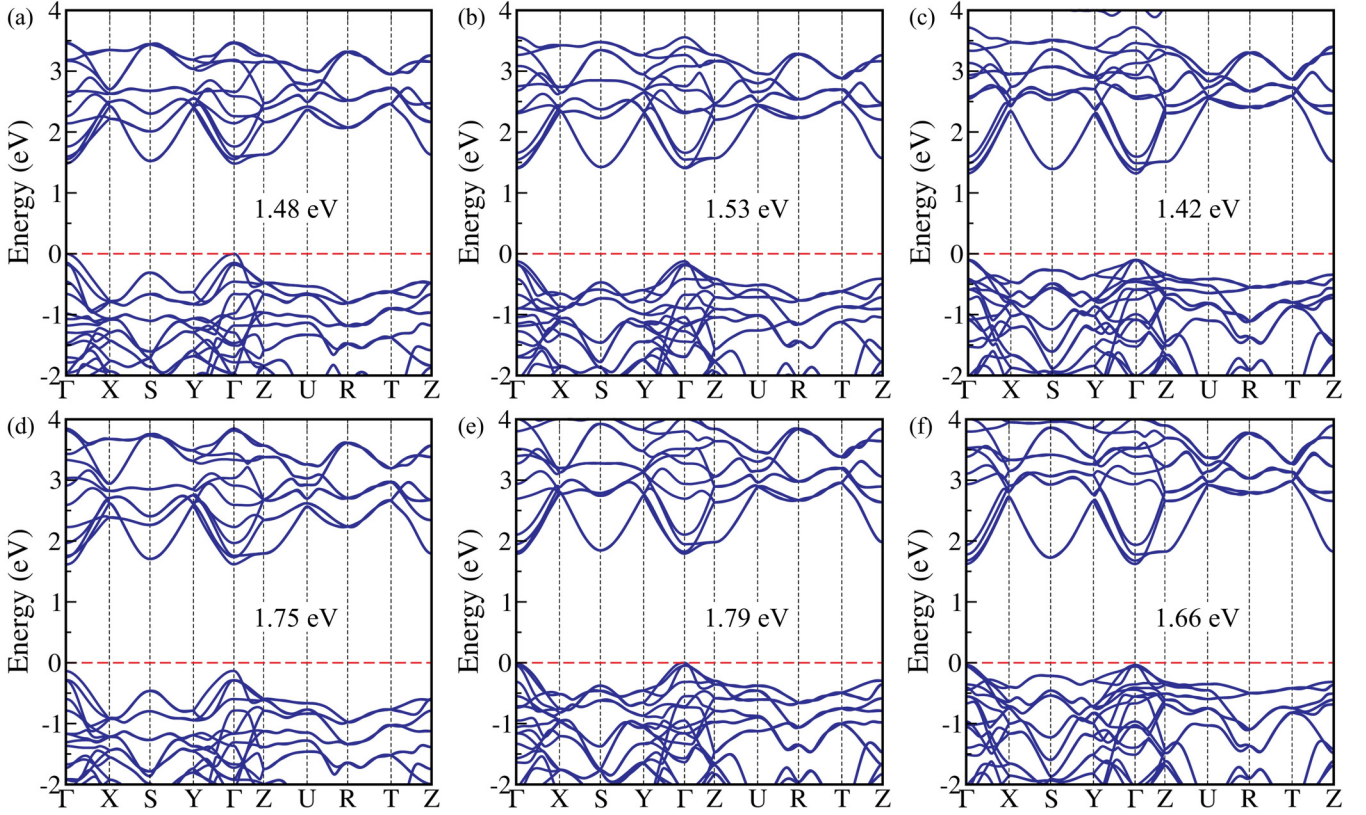


FIG. 3. Electronic band structures of (a) CaZrSe₃, (b) SrZrSe₃, (c) BaZrSe₃, (d) CaHfSe₃, (e) SrHfSe₃, and (f) BaHfSe₃ in orthorhombic distorted (β) phase, obtained using the HSE06 xc functional. The Fermi level is set to be zero and marked by the dashed line.

both the VBM and CBM. The band gap variation of AZrSe₃ perovskites is mainly due to the change in the Zr-Se bond length brought on by replacing Ca with Sr or Ba. Similarly, for the α - and/or β -AHfSe₃ ($A = \text{Ca, Sr, Ba}$) CPs, the VBM mainly consist of the Se-4*p* orbital, but the Hf-5*d* orbital significantly contributes to the CBM. The band gap of Hf-containing compounds increases compared to Zr-containing compounds due to a decrease in the bond length of Hf-Se (2.68 Å) compared to the Zr-Se (3.03 Å) bond length.

To get an insight into charge carrier transport, we further calculated the effective masses of electron (m_e^*) and hole (m_h^*) for all the compounds through the fitted E - k dispersion band diagram of G_0W_0 @PBE band structures using the formula $m^* = \hbar^2[\partial^2 E(k)/\partial k^2]^{-1}$ (for details, see the Supplemental Material [47]). From Table II, it is observed that m_e^* or m_h^* are less than 1 for all the cases, suggesting high carrier mobility and thus better charge carrier transport. The effective masses are also computed using PBE and HSE06 band structures

TABLE II. Band gap (in eV) of chalcogenide perovskites calculated using the PBE, HSE06, and G_0W_0 @PBE method, respectively, as well as computed effective mass of electron (m_e^*) and hole (m_h^*) and reduced mass (μ^*) average along the high-symmetry path $\Gamma - X$, $\Gamma - Y$, and $\Gamma - Z$ directions. Here, t and e represent theoretical and experimental band gaps, respectively, and all values of the effective mass are in terms of free-electron mass (m_0).

Configurations	PBE	HSE06	G_0W_0 @PBE	Previous work	m_e^* (m_0)	m_h^* (m_0)	μ^* (m_0)
CaZrSe ₃	α phase	0.32	1.00	1.19		0.567	0.587
	β phase	0.79	1.48	1.78	1.40 _t [15], 1.43 _t [22]	0.370	0.265
SrZrSe ₃	α phase	0.18	0.86	1.02		0.585	0.390
	β phase	0.83	1.53	1.84	1.46 _t [15], 1.48 _t [22]	0.316	0.269
BaZrSe ₃	α phase	0.39	1.05	1.14	1.11 _t [21]	0.919	0.571
	β phase	0.73	1.42	1.69	1.34 _t [15], 1.37 _t [22]	0.264	0.292
CaHfSe ₃	α phase	0.40	1.10	1.26		0.474	0.501
	β phase	1.05	1.75	1.92		0.358	0.274
SrHfSe ₃	α phase	0.29	0.99	1.09	1.02 _e [19]	0.493	0.360
	β phase	1.10	1.79	1.97		0.345	0.280
BaHfSe ₃	α phase	0.46	1.15	1.18		0.615	0.495
	β phase	0.97	1.66	1.77		0.274	0.395

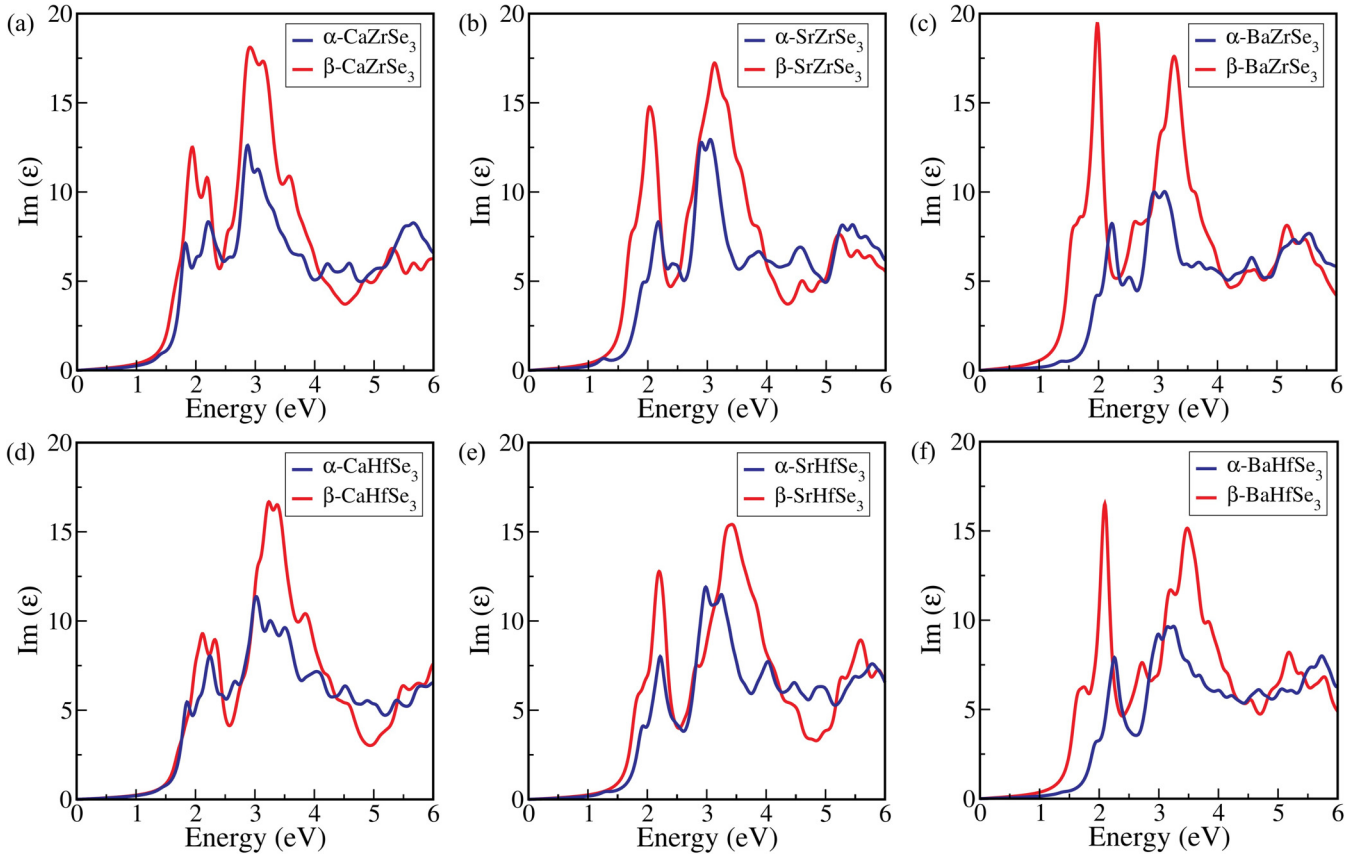


FIG. 4. Imaginary $[\text{Im}(\epsilon)]$ part of the dielectric function of (a) CaZrSe_3 , (b) SrZrSe_3 , (c) BaZrSe_3 , (d) CaHfSe_3 , (e) SrHfSe_3 , and (f) BaHfSe_3 , obtained using the $\text{BSE}@G_0W_0@PBE$ method.

and tabulated in Table S8 of the Supplemental Material [47], which indicates minimal changes in effective masses concerning different functionals.

C. Optical properties

An in-depth investigation of a material's optical characteristics, such as its dielectric function and absorption coefficient, is essential to gain a comprehensive understanding of its suitability for optoelectronic applications. To attain a higher reliability in our estimation, MBPT-based GW -BSE simulations that explicitly account for the electron-hole interactions [39,40] are carried out. To get an optical response, initially, single-shot GW (G_0W_0) [36,37] calculation is performed on the top of PBE and, after that, BSE is solved on the top of $G_0W_0@PBE$. The optical response of the $ABSe_3$ CPs is estimated by calculating the frequency (ω) dependent dielectric function, $\epsilon(\omega) = [\text{Re}(\epsilon)] + i[\text{Im}(\epsilon)]$, where $[\text{Re}(\epsilon)]$ and $[\text{Im}(\epsilon)]$ are the real and imaginary parts of the dielectric function.

The imaginary and real responses of the dielectric function for $ABSe_3$ CPs calculated using the $\text{BSE}@G_0W_0@PBE$ method are depicted in Fig. 4 and Fig. S7, respectively. It is observed that the absorption onset and the first peak position gradually blueshift from α phase to β phase for all investigated CPs. This shift in the absorption onsets corresponds with the rise of the QP band gap in these CPs (see Table II). It should be emphasized that β phases have absorption onset

in the visible region (≥ 1.50 eV), which makes them more favorable for solar cell applications than their respective α phases. Also, the static electronic dielectric constant (ϵ_∞), computed from Fig. S7, is found to increase on going from α phase to β phase (see Table III). Note that a high static dielectric constant leads to a comparatively low charge carrier recombination rate, improving optoelectronic devices' efficiency [66], thereby predicting β -phase CPs to be promising candidates for the optoelectronic applications.

One of the most significant parameters of a material in terms of its photovoltaic use is the absorption coefficient, which provides vital information about the optimal solar energy conversion efficiency. Therefore, the absorption coefficient $[\alpha(\omega)]$ is also calculated for all of the investigated CPs using the following formula [25]:

$$\alpha(\omega) = \sqrt{2}\omega[\sqrt{[\text{Re}(\epsilon)]^2 + [\text{Im}(\epsilon)]^2} - \text{Re}(\epsilon)]^{1/2}. \quad (14)$$

In general, for direct semiconductors [67], the typical $\alpha(\omega)$ in the order of 10^5 cm^{-1} is desirable. As per our $\text{BSE}@G_0W_0@PBE$ results, all of the studied perovskites possess high absorption coefficients (see Fig. S8) that lie in the range of 0.1×10^5 – $1.5 \times 10^5 \text{ cm}^{-1}$.

D. Excitonic properties

The energy required to split an exciton into a single electron (e) and hole (h) pair is known as the exciton binding energy (E_B), which is another important parameter for

TABLE III. Calculated excitonic parameters, phonon screening corrections (ΔE_B^{ph}), and percentage of phonon screening contribution to the reduction of exciton binding energy (%) of chalcogenide perovskites.

Configurations	E_B (meV)	T_{exc} (K)	r_{exc} (nm)	$ \phi_n(0) ^2$ (10^{26} m^{-3})	ΔE_B^{ph} (meV)	%	$(E_B + \Delta E_B^{ph})$ (meV)	
CaZrSe ₃	α phase	98.08	1137	1.46	1.02	-9.83	10.02	88.25
	β phase	33.96	394	3.29	0.09	-9.41	27.71	24.55
SrZrSe ₃	α phase	76.10	882	1.72	0.63	-9.51	12.50	66.59
	β phase	32.69	379	3.47	0.08	-8.93	27.32	23.76
BaZrSe ₃	α phase	109.93	1275	1.02	3.00	-10.33	9.40	99.60
	β phase	30.20	350	3.77	0.06	-8.35	27.65	21.85
CaHfSe ₃	α phase	88.12	1022	1.63	0.74	-8.64	9.80	79.48
	β phase	46.09	534	2.85	0.14	-9.33	20.24	36.76
SrHfSe ₃	α phase	71.69	831	1.85	0.50	-8.25	11.51	63.44
	β phase	43.68	506	2.87	0.14	-9.06	20.74	34.62
BaHfSe ₃	α phase	99.49	1154	1.28	1.52	-9.00	9.05	90.49
	β phase	40.00	464	2.86	0.14	-8.54	21.35	31.46

photovoltaic applications. In photovoltaics, a smaller E_B facilitates easier electron and hole separation, leading to a high photoelectric conversion efficiency. In our study, E_B is computed using the difference between QP band gap and optical band gap obtained from $G_0W_0@PBE$ peak position and BSE@ $G_0W_0@PBE$ peak position, respectively (see Fig. S9). The E_B values (from standard BSE calculations) for $ABSe_3$ CPs are tabulated in Table III. On analyzing the E_B from Table III, it is found that they are relatively lower for β phases compared to α phases. Also, compared to sulfur (S)-based CPs [14,18] ($E_B = 193\text{--}540$ meV), $ABSe_3$ compounds exhibit significantly lower E_B values (30.20–109.93 meV), confirming them to be potential candidates for the application in solar cells.

To have a conclusive estimation of excitonic properties, several excitonic parameters, such as excitonic temperature (T_{exc}), radius (r_{exc}), and probability of wave function [$|\phi_n(0)|^2$] for electron-hole pair at zero charge separation are also computed using Eqs. (4) and (5). The highest temperature at which an exciton may stay stable is known as the excitonic temperature. The thermal energy needed to split an exciton is equal to $E_B = k_B T_{exc}$, where k_B is the Boltzmann constant. Also, the excitonic lifetime (τ_{exc}) can be qualitatively described as the inverse of $|\phi_n(0)|^2$ (for details, see the Supplemental Material [47]). The obtained values of excitonic parameters are tabulated in Table III and it is found that the β phases own a longer exciton lifetime than the α phases, which indicates a lower carrier recombination rate and thus a higher quantum yield and conversion efficiency, in the case of the former.

In comparison to conventional 3D halide perovskites [68], we found a similar range of E_B values in our investigation. The interplay between electronic and ionic contributions to dielectric screening can explain this. Note that, if E_B is significantly more than the longitudinal optical phonon energy ($\hbar\omega_{LO}$), the electronic contribution predominates over the ionic one and the ionic contribution to the dielectric screening remains negligible [69,70]. Since here $E_B \gg \hbar\omega_{LO}$ for all the examined CPs (Tables III and IV), the ionic screening to the dielectric function can be further ignored.

The hydrogenic Wannier-Mott (WM) [18,42] model is also employed to compute the E_B for $ABSe_3$ CPs via Eq. (1), but that requires ϵ_{eff} which is still unknown for these systems (for details, see the Supplemental Material [47]). Therefore, the upper (E_{Bu}) and lower (E_{Bl}) bound for the exciton binding energy are calculated using electronic (ϵ_∞) and static (ϵ_s) contributions to the dielectric constants (Table S10), respectively, as ϵ_{eff} generally lies between both of them.

It is observed that the upper bound of E_B values (listed in Table S10) are almost in agreement with the difference between the peak positions of the GW and BSE (listed in Table III). The standard BSE approach within an *ab initio* framework only captures static screening from electrons to compute the exciton binding energy. This means that the electron-electron interactions that are included in the BSE calculations are based on the static dielectric constant of the material, which accounts for the long-range Coulomb interactions between the charged particles. Nevertheless, this static screening does not account for dynamic electron-electron interactions or the effect of electron-phonon coupling, which can be essential in some materials, especially those in which there is the presence of significant electron-phonon interactions or where phonons play a crucial role in determining optoelectronic properties. Filip and co-workers [45] have recently broadened the discussion to incorporate the phonon screening to the exciton binding energy by deriving a simple expression via Eq. (8). They demonstrated four material specific parameters—the reduced effective mass, static and optical (electronic) dielectric constants, and frequency of the longitudinal optical phonon mode (ω_{LO}), which can be used to reliably predict the magnitude of the phonon screening correction (ΔE_B^{ph}) in isotropic materials. According to Table III, phonon screening substantially lowers the exciton binding energy by 9.05% to 27.71% and is more sensitive for the β phases. This suggests a substantial effect of ionic (or phonon) contribution on the dielectric properties of chalcogenide perovskites. It can be noticed from Table III that the modified values of the exciton binding energy ($E_B + \Delta E_B^{ph}$) are well matched with the upper bound of E_B values for the investigated CPs, in particular, for the β phases.

TABLE IV. Polaron parameters for electrons in chalcogenide perovskites.

Configurations		ω_{LO} (cm ⁻¹)	θ_D (K)	α_e	E_p (meV)	m_p/m^*	μ_p (cm ² V ⁻¹ s ⁻¹)
CaZrSe ₃	α phase	135.33	194.94	1.74	29.85	1.36	32.34
	β phase	115.67	166.61	1.61	23.57	1.33	58.60
SrZrSe ₃	α phase	121.67	175.25	2.13	33.01	1.47	25.25
	β phase	100.00	144.04	1.73	21.93	1.36	67.24
BaZrSe ₃	α phase	114.00	164.21	3.45	50.89	1.87	8.26
	β phase	86.67	124.84	1.74	19.12	1.37	70.68
CaHfSe ₃	α phase	125.33	180.53	1.67	26.51	1.35	42.15
	β phase	118.33	170.45	1.65	24.73	1.34	58.13
SrHfSe ₃	α phase	118.67	170.93	1.85	27.87	1.39	36.47
	β phase	106.33	153.17	1.82	24.56	1.39	56.08
BaHfSe ₃	α phase	112.67	162.29	2.58	37.23	1.60	19.19
	β phase	93.00	133.96	1.78	21.00	1.38	77.59

Further, it should be noted that the current calculations of the exciton binding energy correspond to the $1s$ excitonic peak, while the study of $2s$ and $2p$ excitonic peaks may provide a deeper physical insight into the exciton binding energy of the examined CPs; however, to capture the fine splitting one needs to go for extremely tight convergence parameters, i.e., denser k mesh, in the BSE calculations, and that demands overwhelming computational resources, which are currently beyond our scope. Overall, the investigated distorted phases of $ABSe_3$ CPs are found more suitable for optoelectronic applications, in general, and solar cell technology, in particular, than their needlelike phases.

E. Polaronic properties

As per previous studies [14,18,48], the carrier mobility of polar semiconductors (such as halide and chalcogenide perovskites) is strongly influenced by Fröhlich interactions and this interaction is defined by the dimensionless Fröhlich parameter α [see Eq. (9)]. Therefore, here the interaction of polar optical phonons with the charge carriers is also investigated through the Fröhlich mesoscopic model [48,71,72]. The computed values of α corresponding to electrons and holes are listed in Table IV and Table S12, respectively. The value of $\alpha \ll 1$ generally denotes weak electron (hole)-phonon coupling, whereas $\alpha > 10$ indicates strong coupling [71]. Our results reveal an intermediate electron (hole)-phonon coupling ($\alpha = 1.36$ – 3.45) for our systems of interest.

It should be noted that polaron formation may result in a reduction in the electron and hole quasiparticle (QP) energies and, using α , one can also compute this polaron energy (E_p) through Eq. (10). For α phase (β phase) of CaZrSe₃, SrZrSe₃, BaZrSe₃, CaHfSe₃, SrHfSe₃, and BaHfSe₃, the QP gap is lowered by 60.23 (43.42), 59.85 (42.18), 90.67 (39.25), 53.67 (46.41), 51.59 (46.64), and 70.60 (46.35) meV, respectively. On comparing these values with modified exciton binding energy ($E_B + \Delta E_B^{ph}$), the charge-separated polaronic states of α phases (β phases) are found to be less (more) stable than the bound exciton [14,18].

Other polaron parameters such as effective mass of the polaron (m_p) and polaron mobility (μ_p) are also computed using Eq. (11) and Eq. (12) (for further details, see the Supplemental Material [47]), respectively. On considering the involvement

of optical phonons only, these parameters determine a maximum limit for charge carrier mobilities. If polaron-induced local distortions and acoustic phonon-induced defect scattering are considered, one could anticipate a lowest value of polaron carrier mobility. The calculated m_p values validate the increased carrier-lattice interactions (see Table IV), which explains the lower charge carrier mobility in these cases than the nonpolar or less polar perovskites. The Hellwarth polaron model [46] is used to compute the polaron mobility (μ_p), which is given for electrons and holes in Table IV and Table S12, respectively. It is discovered that these materials exhibit ambipolar characteristics and significantly better polaron mobility for electrons (8.26–77.59 cm²V⁻¹s⁻¹) and holes (19.05–100.49 cm²V⁻¹s⁻¹) than sulfur (S)-based CPs (6.84–18.77 cm²V⁻¹s⁻¹ for electrons and 3.76–6.81 cm²V⁻¹s⁻¹ for holes, respectively) [14,18]. An elucidation of the variances in exciton binding energy and polaron mobility between sulfur (S)- and selenium (Se)-based perovskites is also given in the Supplemental Material [47].

F. Spectroscopic limited maximum efficiency

As discussed above, the β phase of $ABSe_3$ ($A = \text{Ca, Sr, Ba}$; $B = \text{Zr, Hf}$) perovskites exhibits a high absorption coefficient and displays direct band gap in the visible region, predicting them to be effective solar absorbers. To further quantify the photovoltaic performance of these materials, the spectroscopic limited maximum efficiency (SLME) is also estimated, which was introduced by Yu and Zunger [28] (for details, see the Supplemental Material [47]). SLME describes the maximum theoretical limit to the efficiency of the solar power conversion of an absorber material, which is based on an improved version of the Shockley-Queisser (SQ) model [73]. It considers the magnitude and nature of the band gap (direct or indirect), the absorption coefficient of the system, the absorber layer thickness, the material-dependent nonradiative recombination losses, and the temperature. Therefore, the theoretical SLME of $ABSe_3$ perovskites are evaluated at 293.15 K temperature using the standard solar spectrum (AM-1.5G), the absorption coefficient, thickness, and the direct electronic band gap of the material as input.

From the discussion above, it is clear that SLME strongly depends on the band gap's nature. However, it has been seen

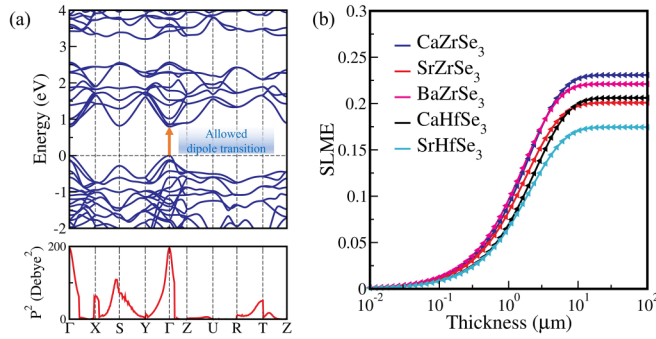


FIG. 5. (a) Electronic band structure and transition probability (square of the transition dipole moment matrix elements) of β -CaZrSe₃ calculated using PBE and (b) spectroscopic limited maximum efficiency of β -ABSe₃ ($A = \text{Ca, Sr, Ba}$; $B = \text{Zr, Hf}$) calculated using BSE@ G_0W_0 @PBE method.

that even after obtaining a direct electronic band gap, the optical transition from VBM to CBM was still forbidden for various perovskites [14,74]. This occurs as a result of the inversion symmetry present in these structures, which causes VBM and CBM to have the same parity. Therefore, to confirm the optical transition possibility from VBM to CBM, the transition dipole moment matrix element is calculated for our systems since its square gives the transition probability between the initial (VBM) state and the final (CBM) state. The square of the transition dipole moment matrix element (P^2) for each system is plotted and presented in Fig. 5(a) and Figs. S10[(a)–(e)] (below their corresponding band structure plots). It is found that β -BaHfSe₃ exhibits a forbidden dipole transition at the Γ point despite having a direct electronic band gap and the rest of the β -ABSe₃ ($A = \text{Ca, Sr, Ba}$; $B = \text{Zr, Hf}$) CPs have allowed dipole transition at the Γ point. Importantly, all α phase of ABSe₃ ($A = \text{Ca, Sr, Ba}$; $B = \text{Zr, Hf}$) CPs also show forbidden dipole transition at the Γ point.

Next, SLME calculations are performed only for systems that have a direct band gap with optically allowed dipole transitions. The calculated SLME of β -ABSe₃ ($A = \text{Ca, Sr, Ba}$; $B = \text{Zr, Hf}$) obtained using BSE@ G_0W_0 @PBE method is shown in Fig. 5(b) and tabulated in Table S13. The SLME values at 10 μm absorber layer thickness are estimated as 23.08%, 20.09%, 22.11%, 20.61%, and 17.45% for β phase of CaZrSe₃, SrZrSe₃, BaZrSe₃, CaHfSe₃, and SrHfSe₃,

respectively. The SLME values clearly reveal that these perovskites are more promising for photovoltaic applications compared to AHfS₃ ($A = \text{Ca, Sr}$), CsGeX₃ ($X = \text{Cl, Br, I}$), and other halide perovskites [14,74–76].

IV. CONCLUSIONS

In summary, we have investigated the ground- and excited-state properties of needlelike (α -phase) and distorted (β -phase) chalcogenide perovskites ABSe₃ ($A = \text{Ca, Sr, Ba}$; $B = \text{Zr, Hf}$) by state-of-the-art density functional theory, density functional perturbation theory, and many-body perturbation theory. Phonon band structures and elastic properties confirm the stability of these perovskites. The electronic G_0W_0 band gaps of the β -ABSe₃ appear in the visible region and calculated effective masses of both carriers are found to be small, suggesting good charge carrier mobility. Following that, the optical properties are well reproduced by solving the Bethe-Salpeter equation (BSE), which indicates a high absorption coefficient for all compounds, and β phases also have absorption onset in the visible region. Additionally, we reveal a negligible ionic contribution to the effective dielectric screening that computes the excitonic parameters. The exciton binding energies that lie in the range of 21.85–99.60 meV are found to be smaller than conventional halide and sulfur-based chalcogenide perovskites. In addition, from Fröhlich’s mesoscopic model, an intermediate electron (hole)-phonon coupling has been observed, which results in higher polaronic mobility in the range of 8.26–77.59 $\text{cm}^2\text{V}^{-1}\text{s}^{-1}$ for electrons and 19.05–100.49 $\text{cm}^2\text{V}^{-1}\text{s}^{-1}$ for holes, and the charge-separated polaronic states of α phases (β phases) are found to be less (more) stable than the bound exciton. In conclusion, the computed spectroscopic limited maximum efficiency which lies in the range $\sim 17.5\%$ –23%, implies β -ABSe₃ could be promising material for photovoltaic applications.

ACKNOWLEDGMENTS

S.A. would like to acknowledge the Council of Scientific and Industrial Research (CSIR), Government of India [Grant No. 09/1128(11453)/2021-EMR-I] for financial support. The high performance computing facility “Magus” and workstations available at the School of Natural Sciences, Shiv Nadar Institution of Eminence, were used to perform all calculations.

[1] A. Kojima, K. Teshima, Y. Shirai, and T. Miyasaka, *J. Am. Chem. Soc.* **131**, 6050 (2009).
 [2] N.-G. Park, *J. Phys. Chem. Lett.* **4**, 2423 (2013).
 [3] J. Berry, T. Buonassisi, D. A. Egger, G. Hodes, L. Kronik, Y.-L. Loo, I. Lubomirsky, S. R. Marder, Y. Mastai, J. S. Miller, D. B. Mitzi, Y. Paz, A. M. Rappe, I. Riess, B. Rybtchinski, O. Stafsudd, V. Stevanovic, M. F. Toney, D. Zitoun, A. Kahn *et al.*, *Adv. Mater.* **27**, 5102 (2015).
 [4] D. A. Egger, A. M. Rappe, and L. Kronik, *Acc. Chem. Res.* **49**, 573 (2016).
 [5] D. B. Straus, S. Guo, A. M. Abeykoon, and R. J. Cava, *Adv. Mater.* **32**, 2001069 (2020).

[6] A. Babayigit, A. Ethirajan, M. Muller, and B. Conings, *Nat. Mater.* **15**, 247 (2016).
 [7] D. Tiwari, O. S. Hutter, and G. Longo, *J. Phys. Energy* **3**, 034010 (2021).
 [8] A. Swarnkar, W. J. Mir, R. Chakraborty, M. Jagadeeswararao, T. Sheikh, and A. Nag, *Chem. Mater.* **31**, 565 (2019).
 [9] K. V. Sopiha, C. Comparotto, J. A. Marquez, and J. J. S. Scragg, *Adv. Opt. Mater.* **10**, 2101704 (2022).
 [10] K. Kuhar, A. Crovetto, M. Pandey, K. S. Thygesen, B. Seger, P. C. K. Vesborg, O. Hansen, I. Chorkendorff, and K. W. Jacobsen, *Energy Environ. Sci.* **10**, 2579 (2017).

- [11] S. Niu, H. Huyan, Y. Liu, M. Yeung, K. Ye, L. Blankemeier, T. Orvis, D. Sarkar, D. J. Singh, R. Kapadia, and J. Ravichandran, *Adv. Mater.* **29**, 1604733 (2017).
- [12] X. Wu, W. Gao, J. Chai, C. Ming, M. Chen, H. Zeng, P. Zhang, S. Zhang, and Y.-Y. Sun, *Sci. China Mater.* **64**, 2976 (2021).
- [13] Y.-Y. Sun, M. L. Agiorgousis, P. Zhang, and S. Zhang, *Nano Lett.* **15**, 581 (2015).
- [14] P. Basera and S. Bhattacharya, *J. Phys. Chem. Lett.* **13**, 6439 (2022).
- [15] D. Liu, H. Zeng, H. Peng, and R. Sa, *Phys. Chem. Chem. Phys.* **25**, 13755 (2023).
- [16] R. Lelieveld and D. J. W. IJdo, *Acta Crystallogr., B* **36**, 2223 (1980).
- [17] C.-S. Lee, K. Kleinke, and H. Kleinke, *Solid State Sci.* **7**, 1049 (2005).
- [18] M. Kumar, A. Singh, D. Gill, and S. Bhattacharya, *J. Phys. Chem. Lett.* **12**, 5301 (2021).
- [19] N. A. Moroz, C. Bauer, L. Williams, A. Olvera, J. Casamento, A. A. Page, T. P. Bailey, A. Weiland, S. S. Stoyko, E. Kioupakis, C. Uher, J. A. Aitken, and P. F. P. Poudeu, *Inorg. Chem.* **57**, 7402 (2018).
- [20] L. J. Tranchitella, B.-H. Chen, J. C. Fettinger, and B. W. Eichhorn, *J. Solid State Chem.* **130**, 20 (1997).
- [21] M. Ong, D. M. Guzman, Q. Campbell, I. Dabo, and R. A. Jishi, *J. Appl. Phys.* **125**, 235702 (2019).
- [22] N. Jaykhedkar, R. Bystricky, M. Sykora, and T. Bucko, *Inorg. Chem.* **62**, 12480 (2023).
- [23] P. Hohenberg and W. Kohn, *Phys. Rev.* **136**, B864 (1964).
- [24] W. Kohn and L. J. Sham, *Phys. Rev.* **140**, A1133 (1965).
- [25] M. Gajdoš, K. Hummer, G. Kresse, J. Furthmüller, and F. Bechstedt, *Phys. Rev. B* **73**, 045112 (2006).
- [26] H. Jiang, P. Rinke, and M. Scheffler, *Phys. Rev. B* **86**, 125115 (2012).
- [27] F. Fuchs, C. Rödl, A. Schleife, and F. Bechstedt, *Phys. Rev. B* **78**, 085103 (2008).
- [28] L. Yu and A. Zunger, *Phys. Rev. Lett.* **108**, 068701 (2012).
- [29] G. Kresse and J. Furthmüller, *Phys. Rev. B* **54**, 11169 (1996).
- [30] G. Kresse and J. Furthmüller, *Comput. Mater. Sci.* **6**, 15 (1996).
- [31] P. E. Blöchl, *Phys. Rev. B* **50**, 17953 (1994).
- [32] J. P. Perdew, K. Burke, and M. Ernzerhof, *Phys. Rev. Lett.* **77**, 3865 (1996).
- [33] K. Momma and F. Izumi, *J. Appl. Crystallogr.* **44**, 1272 (2011).
- [34] A. Togo, L. Chaput, T. Tadano, and I. Tanaka, *J. Phys.: Condens. Matter* **35**, 353001 (2023).
- [35] J. Heyd, G. E. Scuseria, and M. Ernzerhof, *J. Chem. Phys.* **118**, 8207 (2003).
- [36] L. Hedin, *Phys. Rev.* **139**, A796 (1965).
- [37] M. S. Hybertsen and S. G. Louie, *Phys. Rev. Lett.* **55**, 1418 (1985).
- [38] A. M. Ganose, A. J. Jackson, and D. O. Scanlon, *J. Open Source Softw.* **3**, 717 (2018).
- [39] S. Albrecht, L. Reining, R. Del Sole, and G. Onida, *Phys. Rev. Lett.* **80**, 4510 (1998).
- [40] M. Rohlfing and S. G. Louie, *Phys. Rev. Lett.* **81**, 2312 (1998).
- [41] V. Wang, N. Xu, J.-C. Liu, G. Tang, and W.-T. Geng, *Comput. Phys. Commun.* **267**, 108033 (2021).
- [42] S. Adhikari and P. Johari, *Phys. Rev. Mater.* **7**, 075401 (2023).
- [43] J. Kangsabanik, M. K. Svendsen, A. Taghizadeh, A. Crovetto, and K. S. Thygesen, *J. Am. Chem. Soc.* **144**, 19872 (2022).
- [44] X. Gonze and C. Lee, *Phys. Rev. B* **55**, 10355 (1997).
- [45] M. R. Filip, J. B. Haber, and J. B. Neaton, *Phys. Rev. Lett.* **127**, 067401 (2021).
- [46] R. W. Hellwarth and I. Biaggio, *Phys. Rev. B* **60**, 299 (1999).
- [47] See Supplemental Material at <http://link.aps.org/supplemental/10.1103/PhysRevB.109.174114> for the details of crystal structures, bond lengths, dynamical and mechanical stability, effect of spin-orbit coupling on PBE band gaps, total and partial density of states using HSE06, electronic band structures using G_0W_0 @PBE method, details of the effective masses, real part of electronic dielectric function and absorption coefficient using BSE@ G_0W_0 @PBE method, exciton binding energy from standard BSE method and Wannier-Mott model, parameters for calculating the polaron mobility, polaron parameters for holes, and spectroscopic limited maximum efficiency, and it includes Refs. [77–80].
- [48] M. Jain, P. Bhumla, M. Kumar, and S. Bhattacharya, *J. Phys. Chem. C* **126**, 6753 (2022).
- [49] R. P. Feynman, *Phys. Rev.* **97**, 660 (1955).
- [50] J. Xu, J.-B. Liu, J. Wang, B.-X. Liu, and B. Huang, *Adv. Funct. Mater.* **28**, 1800332 (2018).
- [51] C. Li, X. Lu, W. Ding, L. Feng, Y. Gao, and Z. Guo, *Acta Crystallogr.* **64**, 702 (2008).
- [52] G. Volonakis, A. A. Haghighirad, R. L. Milot, W. H. Sio, M. R. Filip, B. Wenger, M. B. Johnston, L. M. Herz, H. J. Snaith, and F. Giustino, *J. Phys. Chem. Lett.* **8**, 772 (2017).
- [53] G. Kieslich, S. Sun, and A. K. Cheetham, *Chem. Sci.* **6**, 3430 (2015).
- [54] P. Bhumla, M. Jain, S. Sheoran, and S. Bhattacharya, *J. Phys. Chem. Lett.* **13**, 11655 (2022).
- [55] A. Jess, R. Yang, and C. J. Hages, *Chem. Mater.* **34**, 6894 (2022).
- [56] E. Osei-Agyemang, C. E. Adu, and G. Balasubramanian, *npj Comput Mater* **5**, 116 (2019).
- [57] F. Mouhat and F.-X. Coudert, *Phys. Rev. B* **90**, 224104 (2014).
- [58] V. Mithal, S. Adhikari, and P. Johari, *Adv. Theory Simul.* **6**, 2200694 (2023).
- [59] Z.-j. Wu, E.-j. Zhao, H.-p. Xiang, X.-f. Hao, X.-j. Liu, and J. Meng, *Phys. Rev. B* **76**, 054115 (2007).
- [60] R. Hill, *Proc. Phys. Soc. A* **65**, 349 (1952).
- [61] S. Pugh, *London, Edinburgh Dublin Philos. Mag. J. Sci.* **45**, 823 (1954).
- [62] M. Mattesini, M. Magnuson, F. Tasnádi, C. Höglund, I. A. Abrikosov, and L. Hultman, *Phys. Rev. B* **79**, 125122 (2009).
- [63] M. Khan, M. Z. Rahaman, and M. L. Ali, *ACS Omega* **8**, 24942 (2023).
- [64] I. Rosa, M. Oliveira, M. Assis, M. Ferrer, R. André, E. Longo, and M. Gurgel, *Ceram. Int.* **41**, 3069 (2015).
- [65] Y. S. Lee, J. S. Lee, T. W. Noh, D. Y. Byun, K. S. Yoo, K. Yamaura, and E. Takayama-Muromachi, *Phys. Rev. B* **67**, 113101 (2003).
- [66] X. Liu, B. Xie, C. Duan, Z. Wang, B. Fan, K. Zhang, B. Lin, F. J. M. Colberts, W. Ma, R. A. J. Janssen, F. Huang, and Y. Cao, *J. Mater. Chem. A* **6**, 395 (2018).
- [67] M. Jain, D. Gill, S. Monga, and S. Bhattacharya, *J. Phys. Chem. C* **127**, 15620 (2023).
- [68] L. M. Herz, *J. Phys. Chem. Lett.* **9**, 6853 (2018).
- [69] M. Bokdam, T. Sander, A. Stroppa, S. Picozzi, D. D. Sarma, C. Franchini, and G. Kresse, *Sci. Rep.* **6**, 28618 (2016).

- [70] C. D. Spataru and F. Leonard, *Chem. Phys.* **413**, 81 (2013).
- [71] J. M. Frost, *Phys. Rev. B* **96**, 195202 (2017).
- [72] H. Fröhlich, *Adv. Phys.* **3**, 325 (1954).
- [73] W. Shockley and H. J. Queisser, *J. Appl. Phys.* **32**, 510 (1961).
- [74] J. Kangsabanik, V. Sugathan, A. Yadav, A. Yella, and A. Alam, *Phys. Rev. Mater.* **2**, 055401 (2018).
- [75] A. C. Dias, M. P. Lima, and J. L. F. Da Silva, *J. Phys. Chem. C* **125**, 19142 (2021).
- [76] J. Qian, B. Xu, and W. Tian, *Org. Electron.* **37**, 61 (2016).
- [77] J. Even, L. Pedesseau, C. Katan, M. Kepenekian, J.-S. Lauret, D. Saponi, and E. Deleporte, *J. Phys. Chem. C* **119**, 10161 (2015).
- [78] K. Ohara, T. Yamada, H. Tahara, T. Aharen, H. Hirori, H. Suzuura, and Y. Kanemitsu, *Phys. Rev. Mater.* **3**, 111601(R) (2019).
- [79] C. D. Spataru, S. Ismail-Beigi, R. B. Capaz, and S. G. Louie, *Phys. Rev. Lett.* **95**, 247402 (2005).
- [80] G. Tang, P. Ghosez, and J. Hong, *J. Phys. Chem. Lett.* **12**, 4227 (2021).